

M3DA: Benchmark for Unsupervised Domain Adaptation in 3D Medical Image Segmentation

Boris Shirokikh

AIRI, Skoltech

shirokikh@airi.net

Anvar Kurmukov

AUMI.AI

Mariia Donskova

IITP RAS

Valentin Samokhin

IITP RAS, AIRI

Mikhail Belyaev

AUMI.AI

Ivan Oseledets

AIRI, Skoltech

oseledets@airi.net

Abstract

Domain shift presents a significant challenge in applying Deep Learning to the segmentation of 3D medical images from sources like Magnetic Resonance Imaging (MRI) and Computed Tomography (CT). Although numerous Domain Adaptation methods have been developed to address this issue, they are often evaluated under impractical data shift scenarios. Specifically, the medical imaging datasets used are often either private, too small for robust training and evaluation, or limited to single or synthetic tasks.

To overcome these limitations, we introduce a M3DA /'medə/ benchmark comprising four publicly available, multiclass segmentation datasets. We have designed eight domain pairs featuring diverse and practically relevant distribution shifts. These include inter-modality shifts between MRI and CT and intra-modality shifts among various MRI acquisition parameters, different CT radiation doses, and presence/absence of contrast enhancement in images.

Within the proposed benchmark, we evaluate more than ten existing domain adaptation methods. Our results show that none of them can consistently close the performance gap between the domains. For instance, the most effective method reduces the performance gap by about 62% across the tasks. This highlights the need for developing novel domain adaptation algorithms to enhance the robustness and scalability of deep learning models in medical imaging.

We made our M3DA benchmark publicly available: <https://github.com/BorisShirokikh/M3DA>.

1. Introduction

Deep Learning (DL) methods have significantly advanced medical image analysis, achieving near-human-level performance in tasks like image classification, segmentation,

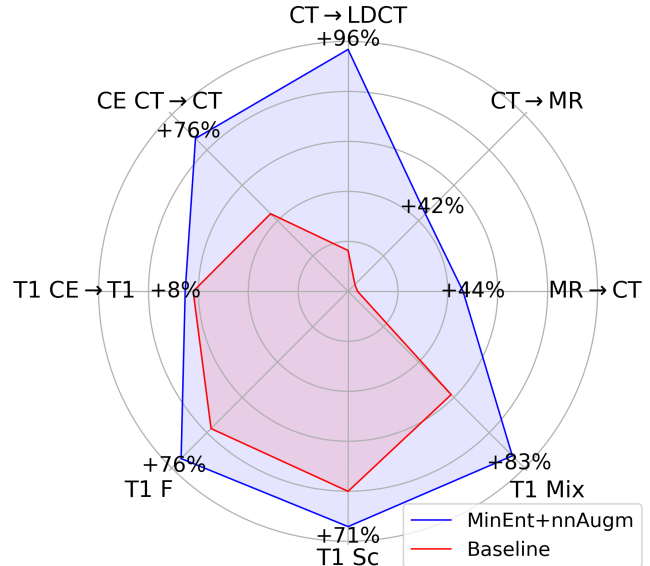


Figure 1. Using the best DA method in the M3DA benchmark closes only 62% of the performance gap between domains on average. Here, % indicates the gap closed between the baseline level and oracle (outer) circle.

pathology detection, and automated diagnosis [36]. However, the widespread adoption of DL in medical imaging is hindered by the poor performance of neural networks on data from distributions different from their training set. This challenge, known as **domain shift**, is particularly prevalent in medical imaging due to changes in scanner acquisition parameters, the introduction of new imaging modalities, and population differences. Several studies have concluded that medical imaging is a crucial domain for the adoption of Domain Adaptation (DA) methods [17, 46, 69, 75, 80]. Despite this, there is a lack of a common benchmark for testing DL methods in the field of 3D medical imaging.

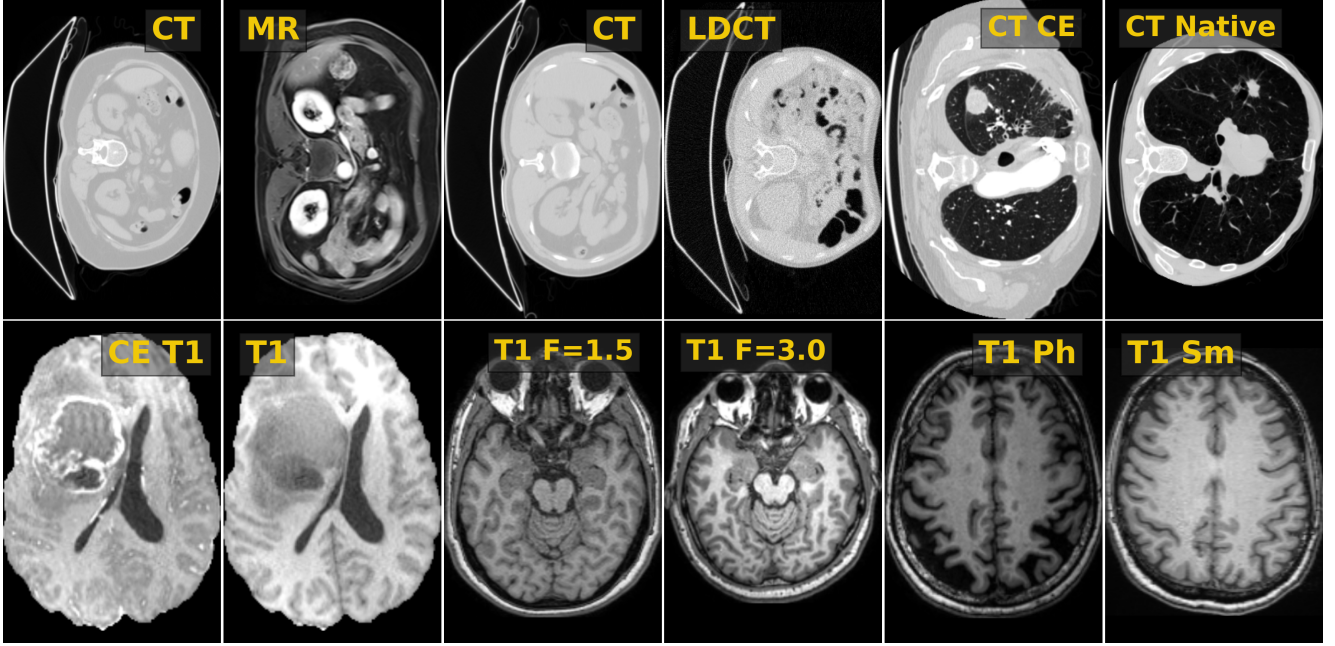


Figure 2. Examples from individual domains in M3DA without segmentation masks for visual comparison between domains. Left to right, top to bottom: CT to MR, CT to LDCT, CT CE to CT native, CE T1 to T1, T1 Field (1.5T to 3T), T1 Scanner (Philips to Siemens). We provide segmentation masks visualization for the same examples in Supplementary materials.

Recent works have focused on developing DA methods, revealing that 3D medical image segmentation algorithms are particularly susceptible to domain shift. Researchers have tested their methods against various sources of domain shift, including shifts between imaging modalities, the most common being MRI and CT [25, 73, 78]. Other sources of domain shift include scanner manufacturers or settings, such as the strength of MR field or CT dosage [8, 15, 32, 38, 47, 78], and intra-modality shifts, such as T2 to T1 MRI [10, 18, 26].

A systematic comparison of these methods, along with the question of the necessity to develop new ones, is complicated by lack of consistency in the usage of datasets across studies, even when addressing similar domain shifts, as shown in Table 1. In addition, many studies test their proposals on a single domain shift problem, limiting the generalizability of their analysis.

Recently, the Cross-Modality Domain Adaptation (CrossMoDA) challenge [10], conducted at MICCAI in 2021 and repeated in 2022 and 2023, attempted to unify various authors under the same framework. The challenge’s setup involved training models on annotated MR T1c with access to unannotated T2 studies, followed by testing on T2 studies. The challenge attracted numerous participants, with the top teams achieving near-supervised performance levels using image-to-image translation techniques paired with multi-stage pseudo-labeling.

Despite its success, the CrossMoDA challenge has cer-

tain limitations. Firstly, it only considers a single source of domain shift, the MR sequence. Secondly, the segmentation task is confined to a two-class challenge: segmenting the vestibular schwannoma tumor and the cochlea, both located in very specific anatomical regions. Consequently, top-performing solutions managed to close up to a 97% score gap between domains. Participants employed various task-specific techniques, such as using only the largest connected component of the segmentation mask to enhance segmentation quality. While this approach may be effective for solving a concrete segmentation task, it is counterproductive for assessing the capabilities of DA methods. It obscures the true impact of adaptation to the unseen domain, hindering a clear understanding of the effectiveness of DA techniques.

Therefore, we conclude that there is a need for a large, diverse, and publicly available benchmark for DA in 3D medical image segmentation that includes a variety of downstream tasks. We introduce such a benchmark to encourage further progress in developing scalable DA methods.

We include four publicly available datasets, encompassing 22 segmentation tasks. Based on these datasets, we construct eight domain adaptation problems; see visual examples of individual domains in Figure 2. Table 3 summarizes all proposed problems with their domain shifts and dataset splits.

To establish a baseline and determine which problems remain unsolved with current methods, we implemented core unsupervised DA (UDA) methods for 3D medical im-

age segmentation. Excluding any task-specific assumptions (e.g., filtering the largest connected component) and human-in-the-loop approaches, the best method within our benchmark closes only 62% of the performance drop between domains on average. Thus, we highlight the need for further development of robust DA methods in 3D medical image segmentation, with our proposed benchmark serving as a strong foundational point for systematically comparing novel methods. We summarize our contributions as follows:

- We propose a benchmark for DA in 3D medical image segmentation that includes eight carefully selected domain shifts based on their practical relevance. These shifts cover variations in imaging modalities, scanner settings, and the presence of contrast agents, ensuring that our benchmark reflects real-world challenges in medical image analysis.
- We provide a comprehensive evaluation of more than ten core domain adaptation methods on our benchmark, covering key categories of UDA approaches.
- Our benchmark is designed to be economical, utilizing only four publicly available datasets. This allows for testing new methods against a wide variety of problems with minimal resources, making our benchmark accessible to researchers and encouraging wider adoption.

2. M3DA Benchmark

We consider a semantic segmentation problem of 3D medical images, which we call a downstream task. Any downstream model works with input samples $x \in X$ and the corresponding segmentation masks $y \in Y$, where X and Y are some input image and label spaces. If $x \in \mathbb{R}^{H \times W \times D}$, segmentation mask is of the same spatial size $y \in \mathbb{R}^{H \times W \times D}$, where every element belongs to a predefined set of labels $y^{(h,w,d)} \in \{0, 1, \dots, C\}$, 0 is background and C is the number of foreground classes.

We follow the standard unsupervised domain adaptation (UDA) problem setting, as in [12]. We assume that two distributions $\mathcal{S}(x, y)$ and $\mathcal{T}(x, y)$ exist on $X \otimes Y$, called *source* and *target* distributions. At the training time, we have a set of source training samples $X^s = \{x_i^s\}_{i=1}^n$ with the corresponding masks $Y^s = \{y_i^s\}_{i=1}^n$ and a set of target training samples X_{tr}^t without annotations; source images and masks are considered to be sampled from \mathcal{S} , $(x_i^s, y_i^s) \sim \mathcal{S}(x, y)$. Our goal is to predict segmentations y given the input from the marginal distribution of target images, $x \sim \mathcal{T}(x)$. To evaluate algorithms, we have target testing samples X_{ts}^t with masks Y_{ts}^t available only for evaluation purposes.

Thus, given domains A and B, one trains a supervised model on domain A while having access to unannotated samples from domain B for adaptation. The goal of UDA is to develop a model that makes accurate predictions on domain B. Importantly, this setup prohibits incorporating annotations from the target domain into the training routine.

2.1. UDA problems motivation

CT \leftrightarrow MRI First, we include domain shift from MRI to CT and vice versa. Although the use of CT scans is often clinically justified, it is associated with additional risks, such as potentially increasing the risk of cancer [5, 7]. In contrast, MRI is a safer imaging modality that does not involve radiation exposure [43]. While CT is critical for various clinical applications like radiotherapy treatment planning, there is a recent transition to MRI for these applications [45]. Thus, developing algorithms that use decades of collected CT data and adapt them for newly acquired MRI scans is an important avenue of research.

The inverse problem of estimating MRI from CT is also an important application. CT is a much faster imaging modality compared to MRI, making it a better solution in emergency scenarios such as stroke. However, MRI provides more sensitive brain visualization [65]. Therefore, having universal algorithms that can adapt to the needed modality at hand is highly beneficial.

While these examples highlight the clinical relevance of domain adaptation between CT and MRI, for the purpose of this benchmark, we utilize a different dataset focusing on thoracic organ segmentation. This choice is motivated by the availability of a dataset that provides both MR and CT images with corresponding segmentation maps for thoracic organs, which is essential for evaluating the performance of UDA algorithms. Despite the difference in the target application, the underlying principles of domain adaptation remain the same, and the insights gained from this benchmark can be applied to various clinical scenarios.

CT \rightarrow low-dose CT Second, we include a CT to low-dose CT (LDCT) shift, motivated by the increasing popularity of LDCT. LDCT produces images with a lower signal-to-noise ratio but are still diagnostically effective, resulting in several-fold lower radiation dosage exposure compared to regular CT (allowing for screening purposes [3, 29]), faster scanning time, mobility to scan underserved populations [51], and cost-effectiveness [42]. Similar to the CT \leftrightarrow MRI domain shift, utilizing publicly available annotated regular CT scans can accelerate the development of automated segmentation models for LDCT. As demonstrated in Table 5, methods trained on regular CT perform poorly on LDCT. This shift is the only one obtained via simulation, where we algorithmically simulate low-dose CT from regular ones.

Contrast enhancement \rightarrow no contrast enhancement Third, we include two tasks, MRI and CT, involving domain transfer from a contrast-enhanced (CE) image to an image without contrast enhancement (native). CE injection is a labor-intensive step, requiring additional training for personnel and carrying a small but additional risk for pa-

Table 1. Comparison to the existing benchmark (CrossMoDA) and datasets that are commonly used for Domain Adaptation in 3D medical image segmentation. Our proposed benchmark (M3DA) covers all primary domain shifts with the largest publicly available datasets.

Paper	Domain shifts	Datasets	Modalities	Region of interest
Jiang et al., 2020 [25]	inter-modality	BTCV, CHAOS	MRI, CT	4 thoracic organs
Al et al., 2021 [1]	inter-modality	MM-WHS	MRI, CT	heart
Weihsbach et al., 2024 [68]	inter-modality	AMOS, MM-WHS, spine	MRI, CT	15 thoracic organs, brain, spine
Liu et al., 2020 [38]	MRI settings, scanners	6 public datasets	MRI	prostate
Gu et al., 2021 [15]	MRI settings, scanners	SAML	MRI	prostate
Chen et al., 2022 [8]	MRI settings, scanners	ACDC, M&Ms	MRI	heart
Lennartz et al., 2023 [32]	MRI settings, scanners	CC359, ACDC, M&Ms	MRI	brain, heart
Wong et al., 2023 [70]	MRI settings, scanners	BraTS	MRI	brain
Liu et al., 2022 [39]	MRI inter-sequence	BraTS	MRI	brain
CrossMoDA, 2023 [10]	MRI inter-sequence	Vestibular Schwannoma	MRI	brain
M3DA (ours)	inter-modality, inter-sequence CT and MRI settings, scanners, contrast	AMOS, CC359, BraTS, LIDC	MRI, CT	brain, tumors, 15 thoracic organs

Table 2. Summary of the datasets commonly used in DA studies. ROI stands for region of interest, and #cls denotes the number of foreground segmentation classes. Several datasets do not contain inner domain shifts, i.e., *single source*; they are used in multi-dataset setups.

Dataset	Modality	ROI	#cls	#cases
WMH [30]	MRI	Brain	2	60
BraTS [41]	MRI	Brain	3	1251
CC359 [56]	MRI	Brain	5	359
ACDC [4]	MRI	Heart	2	150
M&Ms [6]	MRI	Heart	6	375
SCGM [48]	MRI	Spinal Cord	2	80
IVDM3Seg [77]	MRI	Spinal Cord	2	16
BTCV [31]	CT	Abdomen	13	30
AMOS [24]	CT, MRI	Abdomen	15	500, 100
CHAOS [27]	CT, MRI	Thorax	4	50
MM-WHS [81]	CT, MRI	Heart	8	20, 20

tients [2, 9]. Again, we suggest benchmarking DA methods against the scenario where models that utilized richer imaging modalities (CE) during supervised training are adapted for safer modalities (non-contrast-enhanced).

MRI settings Finally, we include three setups that address the domain shifts caused by variable MRI scanner settings, which are among the most common sources of domain shift encountered in practice [34, 71]. These setups cover different field strengths (1.5T vs. 3T), different scanner manufacturers, and a combination of both. Domain shifts arising from variations in scanner settings are ubiquitous in multi-source MRI datasets, as differences in field strength and manufacturer-specific acquisition parameters can significantly impact the appearance and quality of the resulting images. Addressing these shifts is crucial for developing robust and generalizable segmentation models that can handle the heterogeneity of MRI data encountered in real-world clinical scenarios.

2.2. Datasets selection

We base the inclusion of datasets into the benchmark on two criteria. **Relevance**, we aim to cover as many relevant domain shifts as possible; see Section 5.1 for a list of domain shifts not included in our benchmark. **Scale**, we prefer a dataset with a larger number of samples, when deciding between two datasets that are both relevant and include similar domain shifts. All reviewed and selected datasets are summarized in Table 2, and all technical details (e.g., links, download instructions, and licenses) are provided in Supplementary materials.

Table 3. Details of eight tasks in M3DA benchmark. The last three columns correspond to the numbers of cases in *source*, *target train*, and *target test* folds, respectively.

Task name	Domain shift	Dataset	$ X^s $	$ X_{tr}^t $	$ X_{ts}^t $
MR \rightarrow CT	inter-modality	AMOS	60	200	150
CT \rightarrow MR	inter-modality	AMOS	150	40	60
CT \rightarrow LDCT	CT settings	AMOS	150	200	150
CE CT \rightarrow CT	settings (contrast)	LIDC	289	297	297
T1 CE \rightarrow T1	settings (contrast)	BraTS	625	313	313
T1 F	MRI settings	CC359	30	30	30
T1 Sc	MRI scanners	CC359	30	30	30
T1 Mix	settings, scanners	CC359	29	30	30

We start by selecting a dataset for MRI to CT conversion. This allows for several alternatives. Many authors use datasets such as BTCV and CHAOS for these tasks, both of which include images of the thoracic region. BTCV consists of 30 CT scans with 13 organ annotations, and CHAOS of 40 MRI and 40 CT scans with 4 organ annotations. Another option is MM-WHS, which consists of 20 MRI and 20 CT scans of the heart with 8 annotated classes. Finally, there is the newer AMOS dataset, which consists of 500 CT and 100 MRI scans with 15 annotated thoracic organs. Following our criteria, we include AMOS as it is the largest option. We also use AMOS to simulate LDCT data.

To cover CE CT to native CT task, we add Lung Image Database Consortium image collection (LIDC) [3]. LIDC contains chest CT images with and without contrast enhancement with segmentation annotation of lung nodules. LIDC dataset covers lung nodules - an oncology pathology, one of the most common reasons for using contrast enhancement [49]. Then, we cover the similar CE-based data shift in multi-sequence MRI data, from T1 CE to T1 modality. BraTS 2021, being one of the largest and most widely used datasets in the medical imaging community, emerges as the natural choice, satisfying our criteria of relevance, and scale.

Finally, we cover variability in the single-sequence MRI acquisition. As evident from Tables 1 and 2, common choices are the ACDC and M&Ms datasets. Both include segmentation classes of the heart and are relatively large, consisting of 150 and 375 annotated samples, respectively. Both have several concretely defined MRI domains (e.g., different scanners, parameters, field strengths). Another option is CC359, which has the same rich variability in MRI parameters and is similarly sized, including 359 annotated samples. Both ACDC and M&Ms images have $1 \times 1 \times 9 \text{ mm}^3$ spacing, for which a 2D algorithm would often be a more viable choice. In contrast, a significant advantage of CC359 is the fine-grade and consistent voxel spacing, approximately $1 \times 1 \times 1 \text{ mm}^3$, which concludes our selection. UDA setups from the selected datasets are summarized in Table 3.

3. Methods for M3DA Benchmark

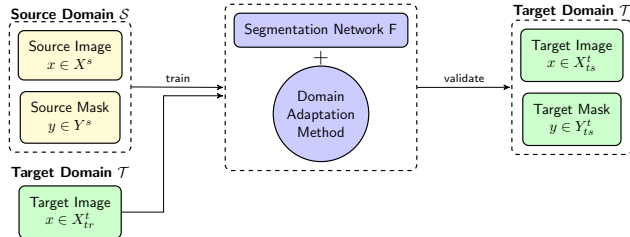


Figure 3. Overview of the UDA pipeline for semantic segmentation. Some methods does not require Target Domain images during training, e.g., nnAugm, IN, AdaBN.

3.1. Segmentation baseline and oracle

Let F be a segmentation network which takes an image $x \in \mathbb{R}^{H \times W \times D}$ and predicts a soft-segmentation map $p = F(x)$, $p \in \mathbb{R}^{H \times W \times D \times (C+1)}$. Here, the last layer of F is softmax which outputs a $(C+1)$ -dimensional voxel-wise vector $[p^{(h,w,d,c)}]_c$ behaving as a discrete distribution over classes. The parameters θ_F of F are learned to minimize some segmentation loss $\mathcal{L}_{seg}(p, y)$. In our case, \mathcal{L}_{seg} is a sum of cross-entropy and Dice losses, as used by default in [22] and many other works. Optimization problem for training on source domain reads:

$$\min_{\theta_F} \frac{1}{|X^s|} \sum_{(x,y) \in (X^s, Y^s)} \mathcal{L}_{seg}(F(x), y). \quad (1)$$

Further, every DA method depends on F , i.e., has the same backbone, so the choice of F is crucial for the benchmark construction. We used the nnU-Net [22] architecture, loss function, and training pipeline, since nnU-Net demonstrated the best performance in several relevant tasks [22–24], including AMOS and BraTS. We also compared nnU-Net to its closest alternatives, UNETR [20], Swin UNETR [19], and MedNeXt [52], directly within our benchmark tasks and confirmed superior nnU-Net performance; see Table 4.

To conduct an ablation study of normalization techniques and nnU-Net pipeline components, we replaced the default instance with batch normalization layers. We also removed modality-specific preprocessing, postprocessing, and test-time augmentations, so we could assess the unhindered impact of DA methods. A detailed technical description is given in Supplementary materials.

An nnU-Net pipeline with the changes above is a backbone for all further experiments; we call it simply U-Net. Finally, we define two core methods of the M3DA benchmark. **Baseline** – U-Net trained on (X^s, Y^s) and tested on (X_{ts}^t, Y_{ts}^t) , i.e., naive transfer. **Oracle** – U-Net trained and tested via cross-validation on (X_{ts}^t, Y_{ts}^t) that might be interpreted as an upper bound estimation for DA methods.

Given baseline and oracle scores, the goal of DA methods therefore is to close the gap between them.

3.2. UDA methods

In our methods selection, we mainly follow reviews of DA for medical image analysis [16, 34]. We include core methods of DA for open-world images, following the corresponding reviews [58, 67, 69], top-performing solutions to the CrossMoDA challenge [10], and most recent Domain Generalization methods [68], totaling 12 methods: Adaptive Batch Normalization (AdaBN) [35], Instance Normalization (IN) [62], Self-ensembling (SE) [11, 47], Minimizing entropy (MinEnt) [64], Domain Adversarial Neural Network (DANN) [12, 26], CycleGAN 2D [79], CycleGAN 3D [76], Histogram matching (HM), nnU-Net augmentations (nnAugm) [22], Gamma correction augmentation (Gamma), Global intensity non-linear (GIN) augmentation [44], and Modality independent neighborhood descriptor (MIND) augmentation [68]. Finally, we include pretrained backbones from foundational models for 3D medical imaging CLIP-driven universal model (UniModel) [37] and SAM-Med3D [66]. A complete description of the methods selection is provided in Supplementary materials.

To ensure fair comparison, we maintained consistent training protocols across all methods, using U-Net backbone from nnU-Net framework for most of the experiments. Most of the DA methods require only minor architectural changes or

no change at all, with only exception being DANN. Implementation details are given in Supplementary materials.

4. Experiments

4.1. Backbone selection

We evaluated four segmentation backbones (U-Net, UNETR, SwinUNETR, and MedNeXt) to determine an optimal baseline architecture for our experiments; see Table 4. For comparison, we included two pretrained models: SAM-Med3D and UniModel, which are based on UNETR and SwinUNETR architectures, respectively, and used officially published model weights.

Table 4. Comparison of various backbones on M3DA benchmark in the *Oracle* setup (training and validating on Target Domain). Numbers are average multiclass Dice score.

	AMOS			LIDC			BraTS		CC359		avgDSC
	CT	MR	LDCT	CT	T1	T1 F	T1 Sc	T1 Mix			
UNETR	0.675	0.791	0.658	0.366	0.559	0.953	0.954	0.957			0.738
SAM-Med3D	0.742	0.813	0.681	0.437	0.473	0.949	0.914	0.951			0.745
MedNeXt	0.869	0.818	0.826	0.000	0.741	0.961	0.964	0.962			0.768
SwinUNETR	0.780	0.791	0.741	0.448	0.660	0.954	0.953	0.957			0.785
UniModel	0.819	0.812	0.776	0.504	0.630	0.955	0.920	0.958			0.797
U-Net	0.842	0.826	0.814	0.519	0.686	0.954	0.957	0.958			0.820
nnU-Net	0.879	0.818	0.848	0.455	0.739	0.963	0.963	0.965			0.829

Our analysis of the foundational models (SAM-Med3D and UniModel) finetuned in supervised fashion yielded three key observations. First, both models demonstrated improved performance compared to their respective base architectures (UNETR and SwinUNETR). Second, we observed that both models slightly underperformed in 4 out of 5 MRI tasks compared to their counterparts trained from scratch, potentially due to their pretraining being predominantly conducted on CT data. Third, neither of them surpassed the performance of a standard U-Net trained from scratch.

MedNeXt performed on par with regular U-Net, however failed to converge on LIDC dataset on multiple runs attempts. Based on these results, we selected the U-Net architecture as our primary backbone.

4.2. Domain Adaptation methods on M3DA

We evaluated various DA methods on the M3DA benchmark (Table 5) using multi-class Dice score and the *percentage of performance gap* closed between the Baseline and Oracle setups: $100 \times \frac{\text{Method}_{\text{Dice}} - \text{Baseline}_{\text{Dice}}}{\text{Oracle}_{\text{Dice}} - \text{Baseline}_{\text{Dice}}}$.

Our analysis begins with non-adapted networks (trained solely on source domain) evaluated on target domain images, represented by three baseline models: U-Net, UniModel (SwinUNETR), and SAM-Med3D (UNETR). Standard U-Net without adaptations failed completely on MR \leftrightarrow CT tasks and showed poor performance on CT tasks (low-dose and CE), while maintaining moderate performance

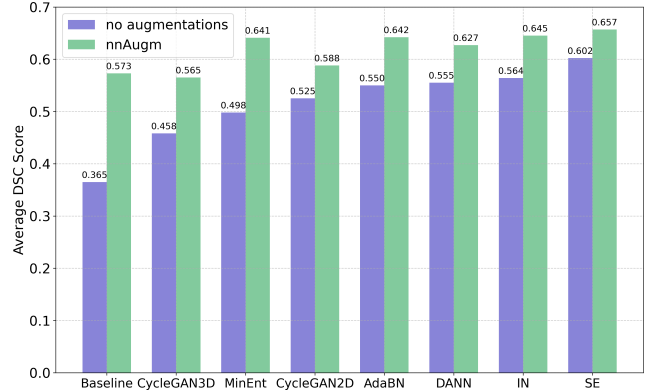


Figure 4. Comparison of DA methods with and without augmentations.

on MRI parameter shift tasks. In contrast, generalist models pretrained using contrastive and segment-anything approaches showed slightly inferior performance on MRI tasks but demonstrated remarkable results on CT-related tasks. Notably, UniModel achieved the best overall performance on the CE CT \rightarrow CT task without adaptations, while SAM-Med3D exhibited strong performance on the CT \rightarrow LDCT task. These results constitute, to our knowledge, the first empirical demonstration of zero-shot domain adaptation capabilities in foundational models for 3D medical imaging.

CycleGANs, despite their success in the CrossMoDA challenge, performed relatively poorly in our benchmark, particularly on CT-based tasks. We attribute this underperformance to the increased complexity of full-resolution CT images compared to brain MRI segmentation, including variations in size, localization regions, fine-grained details, and subtle stylistic differences.

Classical visual UDA methods (AdaBN, InstanceNorm, DANN, and Self-Ensembling) consistently outperformed the baseline, demonstrating their robustness across diverse domain shifts.

Unexpectedly, generic augmentations (nnAugm) and even their subset, Gamma augmentation, outperformed more sophisticated methods on average. This finding strongly suggests the importance of incorporating generic augmentations into DA pipelines, which we explore in the following section.

Finally, recent Domain Generalization methods, GIN and MIND, achieved superior performance on MR \leftrightarrow CT tasks, ranking first and second respectively, with relatively average results across other tasks. We note that these methods were originally developed and evaluated within the MR \leftrightarrow CT setups, so increasing the diversity of a DA benchmark is useful for understanding the true method's capabilities.

4.3. Impact of additional augmentations

Finally, we systematically evaluated the effect of incorporating nnU-Net augmentations, nnAugm, into each domain

Table 5. Main results on our benchmark in terms of multiclass average Dice score, where background label is excluded from quantification. The best results in each column are highlighted in **bold**. Case-wise standard deviations for these experiments are provided in parentheses. Foundational models UniModel and SAM-Med3D were finetuned in the baseline setting, similar to U-Net.

	MR→CT	CT→MR	CT→LDCT	CE CT→CT	T1 CE→T1	T1 F	T1 Sc	T1 Mix	avg DSC	avg gap
U-Net (Baseline)	0.032 (0.045)	0.032 (0.038)	0.133 (0.162)	0.228 (0.265)	0.426 (0.172)	0.741 (0.067)	0.766 (0.025)	0.560 (0.159)	0.365	0.0%
SAM-Med3D [66]	0.019 (0.013)	0.037 (0.031)	0.524 (0.120)	0.412 (0.307)	0.270 (0.155)	0.645 (0.080)	0.758 (0.035)	0.486 (0.274)	0.394	-1.0%
UniModel [37]	0.027 (0.017)	0.012 (0.013)	0.252 (0.191)	0.470 (0.313)	0.331 (0.143)	0.740 (0.064)	0.736 (0.038)	0.618 (0.179)	0.398	7.4%
HM	0.331 (0.182)	0.222 (0.128)	0.111 (0.174)	0.133 (0.221)	0.341 (0.183)	0.789 (0.069)	0.748 (0.090)	0.504 (0.195)	0.397	-1.1%
CycleGAN 3D	0.333 (0.128)	0.264 (0.113)	0.326 (0.175)	0.130 (0.203)	0.345 (0.175)	0.791 (0.035)	0.713 (0.023)	0.762 (0.017)	0.458	9.5%
MinEnt [64]	0.140 (0.136)	0.172 (0.149)	0.505 (0.127)	0.392 (0.323)	0.429 (0.168)	0.770 (0.038)	0.798 (0.025)	0.776 (0.088)	0.498	28.5%
CycleGAN 2D	0.205 (0.153)	0.406 (0.144)	0.530 (0.187)	0.216 (0.260)	0.398 (0.181)	0.852 (0.015)	0.801 (0.027)	0.795 (0.024)	0.525	30.2%
GIN [44]	0.589 (0.144)	0.637 (0.105)	0.722 (0.108)	0.163 (0.238)	0.382 (0.181)	0.837 (0.066)	0.709 (0.069)	0.804 (0.062)	0.605	33.6%
AdaBN [35]	0.322 (0.157)	0.353 (0.177)	0.587 (0.202)	0.295 (0.291)	0.433 (0.165)	0.778 (0.042)	0.833 (0.020)	0.796 (0.059)	0.550	35.0%
DANN [26]	0.296 (0.147)	0.278 (0.135)	0.699 (0.148)	0.409 (0.297)	0.416 (0.161)	0.730 (0.078)	0.833 (0.029)	0.776 (0.082)	0.555	36.2%
IN [62]	0.303 (0.149)	0.308 (0.143)	0.668 (0.167)	0.427 (0.287)	0.428 (0.155)	0.756 (0.058)	0.838 (0.025)	0.784 (0.078)	0.564	39.6%
MIND [68]	0.560 (0.171)	0.588 (0.125)	0.237 (0.148)	0.425 (0.236)	0.335 (0.162)	0.865 (0.035)	0.869 (0.039)	0.845 (0.033)	0.590	45.9%
Gamma	0.349 (0.182)	0.166 (0.146)	0.241 (0.230)	0.441 (0.313)	0.443 (0.163)	0.893 (0.018)	0.910 (0.006)	0.910 (0.012)	0.544	48.3%
SE [47]	0.391 (0.133)	0.388 (0.101)	0.603 (0.189)	0.332 (0.291)	0.388 (0.175)	0.906 (0.023)	0.893 (0.013)	0.918 (0.018)	0.602	51.7%
nnAugm [22]	0.166 (0.125)	0.102 (0.090)	0.779 (0.103)	0.392 (0.315)	0.446 (0.164)	0.910 (0.010)	0.897 (0.012)	0.889 (0.012)	0.573	51.9%
U-Net (Oracle)	0.842 (0.092)	0.826 (0.035)	0.814 (0.095)	0.519 (0.297)	0.686 (0.178)	0.954 (0.017)	0.957 (0.012)	0.958 (0.009)	0.820	100.0%

Table 6. Performance comparison of different methods supplemented with nnU-Net augmentations. Colored numbers show an improvement (or a decline, respectively) over a non-augmented method. GIN and MIND were only trained with nnU-Net augmentations.

	MR→CT	CT→MR	CT→LDCT	CE CT→CT	T1 CE→T1	T1 F	T1 Sc	T1 Mix	avg DSC	avg gap
CycleGAN 3D	0.364 ↑0.031	0.464 ↑0.200	0.679 ↑0.353	0.221 ↑0.091	0.379 ↑0.034	0.825 ↑0.034	0.810 ↑0.097	0.779 ↑0.017	0.565 ↑0.107	34.1% ↑24.6%
CycleGAN 2D	0.301 ↑0.096	0.461 ↑0.055	0.666 ↑0.136	0.333 ↑0.117	0.416 ↑0.018	0.865 ↑0.013	0.850 ↑0.049	0.815 ↑0.020	0.588 ↑0.063	45.5% ↑15.3%
Baseline (nnAugm)	0.166 ↑0.134	0.102 ↑0.070	0.779 ↑0.646	0.392 ↑0.164	0.446 ↑0.020	0.910 ↑0.169	0.897 ↑0.131	0.889 ↑0.329	0.573 ↑0.208	51.9% ↑51.9%
DANN	0.414 ↑0.118	0.349 ↑0.071	0.809 ↑0.110	0.411 ↑0.002	0.403 ↓-0.013	0.899 ↑0.169	0.848 ↑0.015	0.885 ↑0.109	0.627 ↑0.072	54.9% ↑23.3%
IN	0.422 ↑0.119	0.471 ↑0.163	0.796 ↑0.128	0.410 ↓-0.017	0.416 ↓-0.012	0.907 ↑0.151	0.854 ↑0.016	0.883 ↑0.099	0.645 ↑0.081	58.1% ↑26.6%
AdaBN	0.495 ↑0.173	0.532 ↑0.179	0.604 ↑0.017	0.365 ↑0.070	0.454 ↑0.021	0.907 ↑0.129	0.890 ↑0.057	0.892 ↑0.096	0.642 ↑0.092	59.2% ↑24.2%
SE	0.459 ↑0.068	0.571 ↑0.183	0.768 ↑0.165	0.389 ↑0.057	0.374 ↓-0.014	0.902 ↓-0.004	0.907 ↑0.014	0.888 ↓-0.030	0.657 ↑0.055	60.1% ↑8.4%
MinEnt	0.388 ↑0.248	0.362 ↑0.190	0.788 ↑0.283	0.449 ↑0.057	0.448 ↑0.019	0.903 ↑0.133	0.901 ↑0.103	0.892 ↑0.116	0.641 ↑0.143	62.0% ↑33.5%
average	↑0.123	↑0.139	↑0.230	↑0.068	↑0.009	↑0.099	↑0.060	↑0.095	↑0.103	↑26.0%

adaptation method. Our results demonstrate consistent improvements across most methods (Figure 4) and datasets (Table 6), with an average increase of 10.3 percentage points in Dice score. These benefits varied significantly across different domain shifts: CT-related tasks showed the most substantial improvements, while MRI-based tasks exhibited more modest gains.

Different methods also showed varying degrees of improvement when supplemented with augmentations. MinEnt demonstrated the most dramatic enhancement, +33.5 percentage points in average gap, making it the best-performing method overall (Figure 1). CycleGAN-based approaches also benefited significantly, especially in CT-related tasks. Self-Ensembling, while being the strongest initial method, showed the least improvement from the additional augmentations, suggesting that it might already benefited from the incorporated augmentations by design [47]. Notably, some methods exhibited slight performance degradation on specific tasks, indicating that aggressive augmentation strategies may occasionally interfere with method-specific adaptation mechanisms.

Viewing these results from the alternative perspective, we can consider each method as an additional adaptation strat-

egy applied on top of the strong nnAugm baseline. From this point of view, the marginal benefit of adding sophisticated DA methods to an already well-augmented model is more modest but still significant. The best-performing methods (SE and MinEnt) provide an additional 10–15% improvement over nnAugm, demonstrating that DA techniques can capture domain-specific variations that generic augmentations alone cannot address. This suggests that while extensive augmentations should form the foundation of any domain adaptation pipeline, method-specific adaptation mechanisms provide complementary benefits that warrant their inclusion in the final solution.

To conclude, despite significant advances in deep learning over the past decade, our benchmark reveals a concerning trend (Figure 6): DA methods for medical image segmentation have shown minimal improvement since 2017, with recent approaches performing comparably or even worse than earlier ones, suggesting that closing the domain gap remains a fundamental challenge that requires radically new approaches.

5. Discussion

While we focused our computational experiments on unsupervised DA, M3DA also supports other DA frameworks.

Supervised DA involves having annotated data from source and target domains. It can potentially close the performance gap more effectively, leveraging the explicit knowledge of target domain characteristics. All datasets and samples in M3DA come with segmentation annotations, allowing supervised DA setup.

Source-free DA In this setting, the model is trained on the source domain and later adapted to the target domain without accessing source data. This approach is particularly relevant in scenarios with privacy concerns. M3DA allows source-free DA by removing the source data during finetuning.

Test-time DA focuses on adapting the model during inference. This method adjusts to the target domain using only the data available at the inference time. Similar to source-free DA, one can limit access to the source domain and use online sampling of the target data.

Domain Generalization (DG) aims to learn domain-invariant features from multiple source domains without accessing any target domain data during training. This approach is particularly valuable in medical imaging where encountering completely new domains is common, such as images from different hospitals or scanner manufacturers. M3DA’s diverse collection of datasets from various medical centers and imaging protocols¹ makes it well-suited for developing and evaluating DG methods.

These alternative DA frameworks showcase the versatility of our benchmark and its potential to support a wide range of research questions and methodologies in the field of domain adaptation for medical image segmentation.

5.1. Limitations and future directions

While we incorporate a diverse set of domain shifts, our benchmark is not exhaustive. We exclude several candidate domain shifts due to their simplicity, low relevance, or lack of available public data. First, the CT reconstruction kernel (from sinogram space to voxel space) is an important parameter. As shown in [53], this problem can be largely mitigated via simple augmentations or an auxiliary loss function [54]. We include our results on this shift in Supplementary materials, but as it is almost fully addressed by simple augmentations, we exclude it from the main benchmark. Also,

¹LIDC is sourced from seven academic centers and eight medical imaging companies, BraTS is sourced from at least nine different clinical centers, AMOS was collected in two medical centers, from eight different scanners

public datasets containing both reconstruction kernel information and segmentation annotations are scarce.

Second, the CC359 dataset consists of data from six distinct domains, allowing for 30 different domain shift scenarios. We selected the three least “solved” shifts based on our preliminary analysis. A complete table with results on all 30 domain pairs is provided in Supplementary materials.

Third, a common critique of the BraTS dataset is that it is heavily preprocessed. Incorporating raw datasets like Burdenko-GP [82] could provide an evaluation of DA methods in a more realistic setting. However, this comes with an inevitable trade-off of added complexity in data preparation. We also exclude the MRI T1 to T2 domain shift from the main paper. Although we provide the results for this setup in Supplementary materials, we did not find sufficient evidence to support its clinical relevance, leading to its exclusion from our benchmark.

Finally, while the LIDC dataset allows for the CE CT to CT shift, it is primarily designed for object detection tasks, with multiple nodules per image. Despite this limitation, LIDC remains the only publicly available dataset of sufficient size that enables this clinically relevant domain shift.

Future work should focus on expanding M3DA to include more clinically relevant domain shifts, incorporating datasets with unprocessed scans, and exploring novel approaches to domain adaptation.

5.2. Conclusion

In this paper, we introduced the M3DA benchmark for unsupervised domain adaptation in 3D medical image segmentation. Addressing the widely indicated need for developing DA methods in the medical imaging domain [17, 46, 69, 75, 80], we created a large-scale benchmark to facilitate the development of robust segmentation methods in such a crucial application area. Contrary to previously used setups, we covered a diverse set of domain shift sources while using large, publicly available datasets.

We benchmarked the core adaptation methods, covering all key categories of UDA approaches [16, 34], and medical foundational models. Our results revealed that adapted segmentation models struggle to generalize beyond their training distribution when tested at scale. Although some DA methods showed promise in particular settings, we revealed they might completely fail in a number of other setups. This highlights a pressing need for creating robust methods for medical image segmentation, and we hope to foster research efforts in improving adaptation methods’ performance in diverse situations.

Finally, we described several alternative problem settings within M3DA, e.g., supervised and test-time DA, enabling the evaluation of more complex hypotheses across a wider spectrum of DA methods.

References

[1] Dawood Al Chanti and Diana Mateus. Olva: Optimal latent vector alignment for unsupervised domain adaptation in medical image segmentation. In *International Conference on Medical Image Computing and Computer-Assisted Intervention*, pages 261–271. Springer, 2021. 4

[2] Michele Andreucci, Richard Solomon, Adis Tasanarong, et al. Side effects of radiographic contrast media: pathogenesis, risk factors, and prevention. *BioMed research international*, 2014, 2014. 4

[3] Samuel G Armato III, Geoffrey McLennan, Luc Bidaut, Michael F McNitt-Gray, Charles R Meyer, Anthony P Reeves, Binsheng Zhao, Denise R Aberle, Claudia I Henschke, Eric A Hoffman, et al. The lung image database consortium (lidc) and image database resource initiative (idri): a completed reference database of lung nodules on ct scans. *Medical physics*, 38(2):915–931, 2011. 3, 5, 13

[4] Olivier Bernard, Alain Lalande, Clement Zotti, Frederick Cervenansky, Xin Yang, Pheng-Ann Heng, Irem Cetin, Karim Lekadir, Oscar Camara, Miguel Angel Gonzalez Ballester, et al. Deep learning techniques for automatic mri cardiac multi-structures segmentation and diagnosis: is the problem solved? *IEEE transactions on medical imaging*, 37(11):2514–2525, 2018. 4

[5] David J Brenner and Eric J Hall. Computed tomography—an increasing source of radiation exposure. *New England journal of medicine*, 357(22):2277–2284, 2007. 3

[6] Victor M Campello, Polyxeni Gkontra, Cristian Izquierdo, Carlos Martin-Isla, Alireza Sojoudi, Peter M Full, Klaus Maier-Hein, Yao Zhang, Zhiqiang He, Jun Ma, et al. Multi-centre, multi-vendor and multi-disease cardiac segmentation: the m&ms challenge. *IEEE Transactions on Medical Imaging*, 40(12):3543–3554, 2021. 4

[7] Chun-Feng Cao, Kun-Long Ma, Hua Shan, Tang-Fen Liu, Si-Qiao Zhao, Yi Wan, and Hai-Qiang Wang. Ct scans and cancer risks: a systematic review and dose-response meta-analysis. *BMC cancer*, 22(1):1238, 2022. 3

[8] Chen Chen, Zeju Li, Cheng Ouyang, Matthew Sinclair, Wen-jia Bai, and Daniel Rueckert. Maxstyle: Adversarial style composition for robust medical image segmentation. In *International Conference on Medical Image Computing and Computer-Assisted Intervention*, pages 151–161. Springer, 2022. 2, 4

[9] Colleen M Costelloe, Behrang Amini, and John E Madewell. Risks and benefits of gadolinium-based contrast-enhanced mri. In *Seminars in Ultrasound, CT and MRI*, pages 170–182. Elsevier, 2020. 4

[10] Reuben Dorent, Aaron Kujawa, Marina Ivory, Spyridon Bakas, Nicola Rieke, Samuel Joutard, Ben Glocker, Jorge Cardoso, Marc Modat, Kayhan Batmanghelich, et al. Crossmoda 2021 challenge: Benchmark of cross-modality domain adaptation techniques for vestibular schwannoma and cochlea segmentation. *Medical Image Analysis*, 83:102628, 2023. 2, 4, 5, 15

[11] Geoffrey French, Michal Mackiewicz, and Mark Fisher. Self-ensembling for visual domain adaptation. *arXiv preprint arXiv:1706.05208*, 2017. 5, 14

[12] Yaroslav Ganin and Victor Lempitsky. Unsupervised domain adaptation by backpropagation. In *International conference on machine learning*, pages 1180–1189. PMLR, 2015. 3, 5, 15

[13] Muhammad Ghifary, W Bastiaan Kleijn, and Mengjie Zhang. Domain adaptive neural networks for object recognition. In *PRICAI 2014: Trends in Artificial Intelligence: 13th Pacific Rim International Conference on Artificial Intelligence, Gold Coast, QLD, Australia, December 1-5, 2014. Proceedings 13*, pages 898–904. Springer, 2014. 14

[14] Ian Goodfellow, Jean Pouget-Abadie, Mehdi Mirza, Bing Xu, David Warde-Farley, Sherjil Ozair, Aaron Courville, and Yoshua Bengio. Generative adversarial networks. *Communications of the ACM*, 63(11):139–144, 2020. 15

[15] Ran Gu, Jingyang Zhang, Rui Huang, Wenhui Lei, Guotai Wang, and Shaoting Zhang. Domain composition and attention for unseen-domain generalizable medical image segmentation. In *Medical Image Computing and Computer Assisted Intervention—MICCAI 2021: 24th International Conference, Strasbourg, France, September 27–October 1, 2021, Proceedings, Part III 24*, pages 241–250. Springer, 2021. 2, 4

[16] Hao Guan and Mingxia Liu. Domain adaptation for medical image analysis: a survey. *IEEE Transactions on Biomedical Engineering*, 69(3):1173–1185, 2021. 5, 8

[17] Ishaan Gulrajani and David Lopez-Paz. In search of lost domain generalization. *arXiv preprint arXiv:2007.01434*, 2020. 1, 8

[18] Xiaoting Han, Lei Qi, Qian Yu, Ziqi Zhou, Yefeng Zheng, Yinghuan Shi, and Yang Gao. Deep symmetric adaptation network for cross-modality medical image segmentation. *IEEE transactions on medical imaging*, 41(1):121–132, 2021. 2

[19] Ali Hatamizadeh, Vishwesh Nath, Yucheng Tang, Dong Yang, Holger R Roth, and Daguang Xu. Swin unetr: Swin transformers for semantic segmentation of brain tumors in mri images. In *International MICCAI Brainlesion Workshop*, pages 272–284. Springer, 2021. 5

[20] Ali Hatamizadeh, Yucheng Tang, Vishwesh Nath, Dong Yang, Andriy Myronenko, Bennett Landman, Holger R Roth, and Daguang Xu. Unetr: Transformers for 3d medical image segmentation. In *Proceedings of the IEEE/CVF winter conference on applications of computer vision*, pages 574–584, 2022. 5

[21] Sergey Ioffe and Christian Szegedy. Batch normalization: Accelerating deep network training by reducing internal covariate shift. In *International conference on machine learning*, pages 448–456. pmlr, 2015. 14

[22] Fabian Isensee, Paul F Jaeger, Simon AA Kohl, Jens Petersen, and Klaus H Maier-Hein. nnu-net: a self-configuring method for deep learning-based biomedical image segmentation. *Nature methods*, 18(2):203–211, 2021. 5, 7, 15, 16

[23] Fabian Isensee, Tassilo Wald, Constantin Ulrich, Michael Baumgartner, Saikat Roy, Klaus Maier-Hein, and Paul F Jaeger. nnu-net revisited: A call for rigorous validation in 3d medical image segmentation. *arXiv preprint arXiv:2404.09556*, 2024.

[24] Yuanfeng Ji, Haotian Bai, Chongjian Ge, Jie Yang, Ye Zhu, Ruimao Zhang, Zhen Li, Lingyan Zhanng, Wanling Ma, Xiang Wan, et al. Amos: A large-scale abdominal multi-organ

benchmark for versatile medical image segmentation. *Advances in Neural Information Processing Systems*, 35:36722–36732, 2022. 4, 5, 13

[25] Jue Jiang and Harini Veeraraghavan. Unified cross-modality feature disentangler for unsupervised multi-domain mri abdomen organs segmentation. In *Medical Image Computing and Computer Assisted Intervention–MICCAI 2020: 23rd International Conference, Lima, Peru, October 4–8, 2020, Proceedings, Part II 23*, pages 347–358. Springer, 2020. 2, 4

[26] Konstantinos Kamnitsas, Christian Baumgartner, Christian Ledig, Virginia Newcombe, Joanna Simpson, Andrew Kane, David Menon, Aditya Nori, Antonio Criminisi, Daniel Rueckert, et al. Unsupervised domain adaptation in brain lesion segmentation with adversarial networks. In *Information Processing in Medical Imaging: 25th International Conference, IPMI 2017, Boone, NC, USA, June 25–30, 2017, Proceedings 25*, pages 597–609. Springer, 2017. 2, 5, 7, 15, 16

[27] A Emre Kavur, N Sinem Gezer, Mustafa Barış, Sinem Aslan, Pierre-Henri Conze, Vladimir Groza, Duc Duy Pham, Soumick Chatterjee, Philipp Ernst, Savaş Özkan, et al. Chaos challenge-combined (ct-mr) healthy abdominal organ segmentation. *Medical Image Analysis*, 69:101950, 2021. 4

[28] Ekaterina Kondrateva, Polina Druzhinina, Alexandra Dalechina, Svetlana Zolotova, Andrey Golanov, Boris Shirokikh, Mikhail Belyaev, and Anvar Kurmukov. Negligible effect of brain mri data preprocessing for tumor segmentation. *Biomedical Signal Processing and Control*, 96:106599, 2024. 15

[29] Takeshi Kubo, Yoshiharu Ohno, Daisuke Takenaka, Mizuki Nishino, Shiva Gautam, Kazuro Sugimura, Hans Ulrich Kauczor, Hiroto Hatabu, iLEAD Study Group, et al. Standard-dose vs. low-dose ct protocols in the evaluation of localized lung lesions: Capability for lesion characterization—ilead study. *European journal of radiology Open*, 3:67–73, 2016. 3

[30] Hugo J Kuijff, J Matthijs Biesbroek, Jeroen De Bresser, Rutger Heinen, Simon Andermatt, Mariana Bento, Matt Berseth, Mikhail Belyaev, M Jorge Cardoso, Adria Casamitjana, et al. Standardized assessment of automatic segmentation of white matter hyperintensities and results of the wmh segmentation challenge. *IEEE transactions on medical imaging*, 38(11):2556–2568, 2019. 4

[31] Bennett Landman, Zhoubing Xu, J Igelsias, Martin Styner, T Langerak, and Arno Klein. Miccai multi-atlas labeling beyond the cranial vault–workshop and challenge. In *Proc. MICCAI Multi-Atlas Labeling Beyond Cranial Vault—Workshop Challenge*, page 12, 2015. 4

[32] Jonathan Lennartz and Thomas Schultz. Segmentation distortion: Quantifying segmentation uncertainty under domain shift via the effects of anomalous activations. In *International Conference on Medical Image Computing and Computer-Assisted Intervention*, pages 316–325. Springer, 2023. 2, 4

[33] Johannes Leuschner, Maximilian Schmidt, Daniel Otero Baquer, and Peter Maass. Lodopab-ct, a benchmark dataset for low-dose computed tomography reconstruction. *Scientific Data*, 8(1):109, 2021. 13

[34] Yuemeng Li and Yong Fan. Medical image segmentation with domain adaptation: A survey. *arXiv preprint arXiv:2311.01702*, 2023. 4, 5, 8

[35] Yanghao Li, Naiyan Wang, Jianping Shi, Xiaodi Hou, and Jiaying Liu. Adaptive batch normalization for practical domain adaptation. *Pattern Recognition*, 80:109–117, 2018. 5, 7, 14

[36] Geert Litjens, Thijs Kooi, Babak Ehteshami Bejnordi, Arnaud Arindra Adiyoso Setio, Francesco Ciompi, Mohsen Ghafoorian, Jeroen Awm Van Der Laak, Bram Van Ginneken, and Clara I Sánchez. A survey on deep learning in medical image analysis. *Medical image analysis*, 42:60–88, 2017. 1

[37] Jie Liu, Yixiao Zhang, Jie-Neng Chen, Junfei Xiao, Yongyi Lu, Bennett A Landman, Yixuan Yuan, Alan Yuille, Yucheng Tang, and Zongwei Zhou. Clip-driven universal model for organ segmentation and tumor detection. In *Proceedings of the IEEE/CVF International Conference on Computer Vision*, pages 21152–21164, 2023. 5, 7

[38] Quande Liu, Qi Dou, and Pheng-Ann Heng. Shape-aware meta-learning for generalizing prostate mri segmentation to unseen domains. In *Medical Image Computing and Computer Assisted Intervention–MICCAI 2020: 23rd International Conference, Lima, Peru, October 4–8, 2020, Proceedings, Part II 23*, pages 475–485. Springer, 2020. 2, 4

[39] Xiaofeng Liu, Fangxu Xing, Nadya Shusharina, Ruth Lim, C-C Jay Kuo, Georges El Fakhri, and Jonghye Woo. Act: Semi-supervised domain-adaptive medical image segmentation with asymmetric co-training. In *International Conference on Medical Image Computing and Computer-Assisted Intervention*, pages 66–76. Springer, 2022. 4

[40] Mingsheng Long, Yue Cao, Jianmin Wang, and Michael Jordan. Learning transferable features with deep adaptation networks. In *International conference on machine learning*, pages 97–105. PMLR, 2015. 14

[41] Bjoern H Menze, Andras Jakab, Stefan Bauer, Jayashree Kalpathy-Cramer, Keyvan Farahani, Justin Kirby, Yuliya Burren, Nicole Porz, Johannes Slotboom, Roland Wiest, et al. The multimodal brain tumor image segmentation benchmark (brats). *IEEE transactions on medical imaging*, 34(10):1993–2024, 2014. 4, 13

[42] Marita Mohammadshahi, Minoo Alipouri Sakha, Atefeh Esfandiari, Maryam Shirvani, and Ali Akbari Sari. Cost effectiveness of mobile versus fixed computed tomography and magnetic resonance imaging: a systematic review. *Iranian Journal of Public Health*, 48(8):1418, 2019. 3

[43] Dong Nie, Xiaohuan Cao, Yaozong Gao, Li Wang, and Dinggang Shen. Estimating ct image from mri data using 3d fully convolutional networks. In *Deep Learning and Data Labeling for Medical Applications: First International Workshop, LABELS 2016, and Second International Workshop, DLMIA 2016, Held in Conjunction with MICCAI 2016, Athens, Greece, October 21, 2016, Proceedings 1*, pages 170–178. Springer, 2016. 3

[44] Cheng Ouyang, Chen Chen, Surui Li, Zeju Li, Chen Qin, Wenjia Bai, and Daniel Rueckert. Causality-inspired single-source domain generalization for medical image segmentation. *IEEE Transactions on Medical Imaging*, 42(4):1095–1106, 2022. 5, 7, 15, 16

[45] Viktor R Paczona, Marta E Capala, Borbála Deák-Karancsi, Emőke Borzásı, Zsófia Együd, Zoltán Végváry, Gyöngyi Kelemen, Renáta Kószó, László Ruskó, Lehel Ferenczi, et al.

Magnetic resonance imaging-based delineation of organs at risk in the head and neck region. *Advances in Radiation Oncology*, 8(2):101042, 2023. 3

[46] Xingchao Peng, Ben Usman, Neela Kaushik, Dequan Wang, Judy Hoffman, and Kate Saenko. Visda: A synthetic-to-real benchmark for visual domain adaptation. In *Proceedings of the IEEE Conference on Computer Vision and Pattern Recognition Workshops*, pages 2021–2026, 2018. 1, 8

[47] Christian S Perone, Pedro Ballester, Rodrigo C Barros, and Julien Cohen-Adad. Unsupervised domain adaptation for medical imaging segmentation with self-ensembling. *NeuroImage*, 194:1–11, 2019. 2, 5, 7, 14, 15, 16

[48] Ferran Prados, John Ashburner, Claudia Blaiotta, Tom Brosch, Julio Carballido-Gamio, Manuel Jorge Cardoso, Benjamin N Conrad, Esha Datta, Gergely Dávid, Benjamin De Leener, et al. Spinal cord grey matter segmentation challenge. *NeuroImage*, 152:312–329, 2017. 4

[49] Camila Piza Purysko, Rahul Renapurkar, and Michael A Bolen. When does chest ct require contrast enhancement? *Cleveland Clinic Journal of Medicine*, 83(6):423–426, 2016. 5, 14

[50] Alec Radford, Luke Metz, and Soumith Chintala. Unsupervised representation learning with deep convolutional generative adversarial networks. *arXiv preprint arXiv:1511.06434*, 2015. 16

[51] Derek Raghavan, Mellisa Wheeler, Darcy Doege, John D Doty, Henri Levy, Kia A Dungan, Lauren M Davis, James M Robinson, Edward S Kim, Kathryn F Mileham, et al. Initial results from mobile low-dose computerized tomographic lung cancer screening unit: improved outcomes for underserved populations. *The oncologist*, 25(5):e777–e781, 2020. 3

[52] Saikat Roy, Gregor Koehler, Constantin Ulrich, Michael Baumgartner, Jens Petersen, Fabian Isensee, Paul F Jaeger, and Klaus H Maier-Hein. Mednext: transformer-driven scaling of convnets for medical image segmentation. In *International Conference on Medical Image Computing and Computer-Assisted Intervention*, pages 405–415. Springer, 2023. 5

[53] Talgat Saparov, Anvar Kurmukov, Boris Shirokikh, and Mikhail Belyaev. Zero-shot domain adaptation in ct segmentation by filtered back projection augmentation. In *Deep Generative Models, and Data Augmentation, Labelling, and Imperfections: First Workshop, DGM4MICCAI 2021, and First Workshop, DALI 2021, Held in Conjunction with MICCAI 2021, Strasbourg, France, October 1, 2021, Proceedings 1*, pages 243–250. Springer, 2021. 8, 15

[54] Stanislav Shimovolos, Andrey Shushko, Mikhail Belyaev, and Boris Shirokikh. Adaptation to ct reconstruction kernels by enforcing cross-domain feature maps consistency. *Journal of Imaging*, 8(9):234, 2022. 8

[55] Boris Shirokikh, Ivan Zakazov, Alexey Chernyavskiy, Irina Fedulova, and Mikhail Belyaev. First u-net layers contain more domain specific information than the last ones. In *Domain Adaptation and Representation Transfer, and Distributed and Collaborative Learning: Second MICCAI Workshop, DART 2020, and First MICCAI Workshop, DCL 2020, Held in Conjunction with MICCAI 2020, Lima, Peru, October 4–8, 2020, Proceedings 2*, pages 117–126. Springer, 2020. 13

[56] Roberto Souza, Oeslle Lucena, Julia Garrafa, David Gobbi, Marina Saluzzi, Simone Appenzeller, Letícia Rittner, Richard Frayne, and Roberto Lotufo. An open, multi-vendor, multi-field-strength brain mr dataset and analysis of publicly available skull stripping methods agreement. *NeuroImage*, 170: 482–494, 2018. 4, 13

[57] Baochen Sun, Jiashi Feng, and Kate Saenko. Return of frustratingly easy domain adaptation. In *Proceedings of the AAAI conference on artificial intelligence*, 2016. 14

[58] Marco Toldo, Andrea Maracani, Umberto Michieli, and Pietro Zanuttigh. Unsupervised domain adaptation in semantic segmentation: a review. *Technologies*, 8(2):35, 2020. 5, 15

[59] Yi-Hsuan Tsai, Wei-Chih Hung, Samuel Schulter, Kihyuk Sohn, Ming-Hsuan Yang, and Manmohan Chandraker. Learning to adapt structured output space for semantic segmentation. In *Proceedings of the IEEE conference on computer vision and pattern recognition*, pages 7472–7481, 2018. 15

[60] Eric Tzeng, Judy Hoffman, Ning Zhang, Kate Saenko, and Trevor Darrell. Deep domain confusion: Maximizing for domain invariance. *arXiv preprint arXiv:1412.3474*, 2014. 14

[61] Eric Tzeng, Judy Hoffman, Kate Saenko, and Trevor Darrell. Adversarial discriminative domain adaptation. In *Proceedings of the IEEE conference on computer vision and pattern recognition*, pages 7167–7176, 2017. 15

[62] Dmitry Ulyanov, Andrea Vedaldi, and Victor Lempitsky. Improved texture networks: Maximizing quality and diversity in feed-forward stylization and texture synthesis. In *Proceedings of the IEEE conference on computer vision and pattern recognition*, pages 6924–6932, 2017. 5, 7, 14

[63] Anton Vasiliuk, Daria Frolova, Mikhail Belyaev, and Boris Shirokikh. Limitations of out-of-distribution detection in 3d medical image segmentation. *Journal of Imaging*, 9(9), 2023. 15

[64] Tuan-Hung Vu, Himalaya Jain, Maxime Bucher, Matthieu Cord, and Patrick Pérez. Advent: Adversarial entropy minimization for domain adaptation in semantic segmentation. In *Proceedings of the IEEE/CVF Conference on Computer Vision and Pattern Recognition*, pages 2517–2526, 2019. 5, 7, 14, 16

[65] Josef Vymazal, Aaron M Rulseh, Jiří Keller, and Ladislava Janouskova. Comparison of ct and mr imaging in ischemic stroke. *Insights into imaging*, 3:619–627, 2012. 3

[66] Haoyu Wang, Sizheng Guo, Jin Ye, Zhongying Deng, Junlong Cheng, Tianbin Li, Jianpin Chen, Yanzhou Su, Ziyan Huang, Yiqing Shen, Bin Fu, Shaoting Zhang, Junjun He, and Yu Qiao. Sam-med3d: Towards general-purpose segmentation models for volumetric medical images, 2024. 5, 7

[67] M. Wang and Weihong Deng. Deep visual domain adaptation: A survey. *Neurocomputing*, 312:135–153, 2018. 5

[68] Christian Weihsbach, Christian N Kruse, Alexander Bigalke, and Mattias P Heinrich. Dg-tta: Out-of-domain medical image segmentation through domain generalization and test-time adaptation. *arXiv preprint arXiv:2312.06275*, 2023. 4, 5, 7, 15, 16

[69] Garrett Wilson and Diane J Cook. A survey of unsupervised deep domain adaptation. *ACM Transactions on Intelligent Systems and Technology (TIST)*, 11(5):1–46, 2020. 1, 5, 8

[70] Ken CL Wong, Hongzhi Wang, and Tanveer Syeda-Mahmood. Hartleymha: Self-attention in frequency domain for resolution-robust and parameter-efficient 3d image segmentation. In *International Conference on Medical Image Computing and Computer-Assisted Intervention*, pages 364–373. Springer, 2023. [4](#)

[71] Wenjun Yan, Lu Huang, Liming Xia, Shengjia Gu, Fuhua Yan, Yuanyuan Wang, and Qian Tao. Mri manufacturer shift and adaptation: increasing the generalizability of deep learning segmentation for mr images acquired with different scanners. *Radiology: Artificial Intelligence*, 2(4):e190195, 2020. [4](#)

[72] Yanchao Yang and Stefano Soatto. Fda: Fourier domain adaptation for semantic segmentation. In *Proceedings of the IEEE/CVF Conference on Computer Vision and Pattern Recognition*, pages 4085–4095, 2020. [15](#)

[73] Qinji Yu, Nan Xi, Junsong Yuan, Ziyu Zhou, Kang Dang, and Xiaowei Ding. Source-free domain adaptation for medical image segmentation via prototype-anchored feature alignment and contrastive learning. In *International Conference on Medical Image Computing and Computer-Assisted Intervention*, pages 3–12. Springer, 2023. [2](#)

[74] Ivan Zakazov, Vladimir Shaposhnikov, Iaroslav Bespalov, and Dmitry V Dylov. Feather-light fourier domain adaptation in magnetic resonance imaging. In *Domain Adaptation and Representation Transfer: 4th MICCAI Workshop, DART 2022, Held in Conjunction with MICCAI 2022, Singapore, September 22, 2022, Proceedings*, pages 88–97. Springer, 2022. [15](#)

[75] Haoran Zhang, Natalie Dullerud, Laleh Seyyed-Kalantari, Quaid Morris, Shalmali Joshi, and Marzyeh Ghassemi. An empirical framework for domain generalization in clinical settings. In *Proceedings of the conference on health, inference, and learning*, pages 279–290, 2021. [1, 8](#)

[76] Zizhao Zhang, Lin Yang, and Yefeng Zheng. Translating and segmenting multimodal medical volumes with cycle-and shape-consistency generative adversarial network. In *Proceedings of the IEEE conference on computer vision and pattern Recognition*, pages 9242–9251, 2018. [5, 15, 16](#)

[77] Guoyan Zheng, Daniel Belavy, and Shuo Li. IVDM3Seg Dataset. <https://ivdm3seg.weebly.com/data.html>, 2018. Accessed: [insert date of access]. [4](#)

[78] Hao Zheng, Jun Han, Hongxiao Wang, Lin Yang, Zhuo Zhao, Chaoli Wang, and Danny Z Chen. Hierarchical self-supervised learning for medical image segmentation based on multi-domain data aggregation. In *Medical Image Computing and Computer Assisted Intervention–MICCAI 2021: 24th International Conference, Strasbourg, France, September 27–October 1, 2021, Proceedings, Part I* 24, pages 622–632. Springer, 2021. [2](#)

[79] Jun-Yan Zhu, Taesung Park, Phillip Isola, and Alexei A Efros. Unpaired image-to-image translation using cycle-consistent adversarial networks. In *Proceedings of the IEEE international conference on computer vision*, pages 2223–2232, 2017. [5, 15, 16](#)

[80] Fuzhen Zhuang, Zhiyuan Qi, Keyu Duan, Dongbo Xi, Yongchun Zhu, Hengshu Zhu, Hui Xiong, and Qing He. A comprehensive survey on transfer learning. *Proceedings of the IEEE*, 109(1):43–76, 2020. [1, 8](#)

[81] Xiahai Zhuang and Juan Shen. Multi-scale patch and multi-modality atlases for whole heart segmentation of mri. *Medical image analysis*, 31:77–87, 2016. [4](#)

[82] S. V. Zolotova, A. V. Golanov, I. N. Pronin, A. V. Dalechina, A. A. Nikolaeva, A. S. Belyashova, D. Y. Usachev, E. A. Kondrateva, P. V. Druzhinina, B. N. Shirokikh, T. N. Saparov, M. G. Belyaev, and A. I. Kurmukov. Burdenko’s glioblastoma progression dataset (burdenko-gbm-progression), 2023. [8](#)

[83] Yang Zou, Zhiding Yu, BVK Kumar, and Jinsong Wang. Unsupervised domain adaptation for semantic segmentation via class-balanced self-training. In *Proceedings of the European conference on computer vision (ECCV)*, pages 289–305, 2018. [14](#)

M3DA: Benchmark for Unsupervised Domain Adaptation in 3D Medical Image Segmentation

Supplementary Material

6. Datasets description

Below we provide an extended description of datasets used in M3DA benchmark, download and usage examples are available at <https://github.com/BorisShirokikh/M3DA>. Example 2D slices from every dataset for visual comparison between domains are given in Figure 5. Summary of licenses and data access is given in Table 7.

Table 7. Datasets licenses and independent source links.

Dataset	license	link to dataset
BraTS [41]	CC BY 4.0	https://www.cancerimagingarchive.net/analysis-result/rsna-asnr-miccai-brats-2021/
CC359 [56]	CC BY-ND 4.0	https://www.ccdataset.com/download
AMOS [24]	CC BY 4.0	https://zenodo.org/records/7262581
AMOS LDCT	CC BY 4.0	https://zenodo.org/records/13373720
LIDC [3]	CC BY 3.0	https://www.cancerimagingarchive.net/collection/lidc-idri/

6.1. AMOS

The AMOS dataset [24] contains 500 CT and 100 MRI abdominal scans with the multi-organ segmentation task: liver, stomach, spleen, left and right kidneys, bladder, aorta, pancreas, inferior vena cava, duodenum, prostate/uterus, gall-bladder, esophagus, left and right adrenals. As a largest available dataset for inter-modality segmentation, we employed it in MR→CT and CT→MR domain shift setups.

Furthermore, we used AMOS CT images to create one of the most clinically relevant domain shift setups – difference in the radiation dose during scanning.

For the LDCT domain, we simulated low radiation dose using the algorithm provided in [33], simulated data are available at <https://zenodo.org/records/13373720>.

6.2. BraTS

BraTS [41] is comprised of 2000 brain MRI cases, each consisting of four sequences: T1, T1c, T2, FLAIR, with a glioblastoma segmentation classes (3 foreground classes and background). We only used 1251 cases with publicly available annotations and T1, T1c MRI sequences for T1 CE→T1 shift. Since sequences of the same case provide information about the same subject, we ensured source-target splits so that every case falls into exactly one fold.

6.3. CC359

The CC359 dataset [56] contains 359 brain MR T1 images from three scanners, namely, GE, Philips (PH), and Siemens (SM), obtained using two magnetic field strength values, 1.5 and 3.0T. The dataset can be split into six domains defined by two different field strengths × three vendors, each with

approximately 60 images, so it yields 30 possible domain adaptation pairs.

CC359 also offers three tasks: brain, hippocampus, and white matter, gray matter, and cerebrospinal fluid (WMGM-CSF) segmentation. We omitted hippocampus segmentation task from the benchmark, because our preliminary experiments showed it is not significantly affected by domain shifts, the relative performance drop is less than 2% in every domain pair; see Table 8. We also omitted the brain segmentation task for the same reason, see results in [55].

Table 8. Baseline and oracle results on the CC359 hippocampus segmentation task.

		Target domains					
		GE1.5	PH1.5	SM1.5	GE3.0	PH3.0	SM3.0
Source domains	GE 1.5	92.3	86.7	88.7	87.8	91.2	91.2
	PH 1.5	91.3	86.9	87.7	87.7	89.7	89.9
	SM 1.5	91.7	86.6	89.3	88.2	90.9	90.8
	GE 3.0	91.4	86.4	88.0	89.1	90.5	91.3
	PH 3.0	91.5	86.5	88.3	87.7	92.0	91.0
	SM 3.0	90.8	86.5	87.8	88.0	90.6	92.1

Therefore, we focus only on the WMGMCSF segmentation task in CC359: white matter, gray matter and cerebral spinal fluid segmentation classes and background. From 30 possible domain pairs, we selected three with the maximum performance drop, highlighted in **bold**, Table 9): changing field strength with a fixed scanner PH 1.5T → PH 3.0T (drop from 95.4 to 74.1 Dice score), changing scanner with the fixed field strength PH 3.0T → SM 3.0T (drop from 95.7 to 76.6), and changing both parameters SM 3.0T → GE 1.5T (drop from 95.8 to 56.0). We denote them as T1 F, T1 Sc, and T1 Mix, respectively.

Table 9. Baseline and oracle results on the CC359 WMGMSCF segmentation task.

		Target domains					
		GE1.5	PH1.5	SM1.5	GE3.0	PH3.0	SM3.0
Source domains	GE 1.5	95.8	82.1	90.8	82.1	92.6	80.8
	PH 1.5	80.1	92.7	90.8	93.4	74.1	90.1
	SM 1.5	89.7	85.3	95.6	86.2	86.2	84.5
	GE 3.0	76.6	89.9	90.3	95.9	72.0	91.4
	PH 3.0	90.6	74.7	86.0	75.4	95.4	76.6
	SM 3.0	56.0	88.6	84.9	92.4	68.4	95.7

6.4. LIDC

LIDC [3] is a multi-center collection of diagnostic and lung cancer screening thoracic CT scans with annotated lesions.

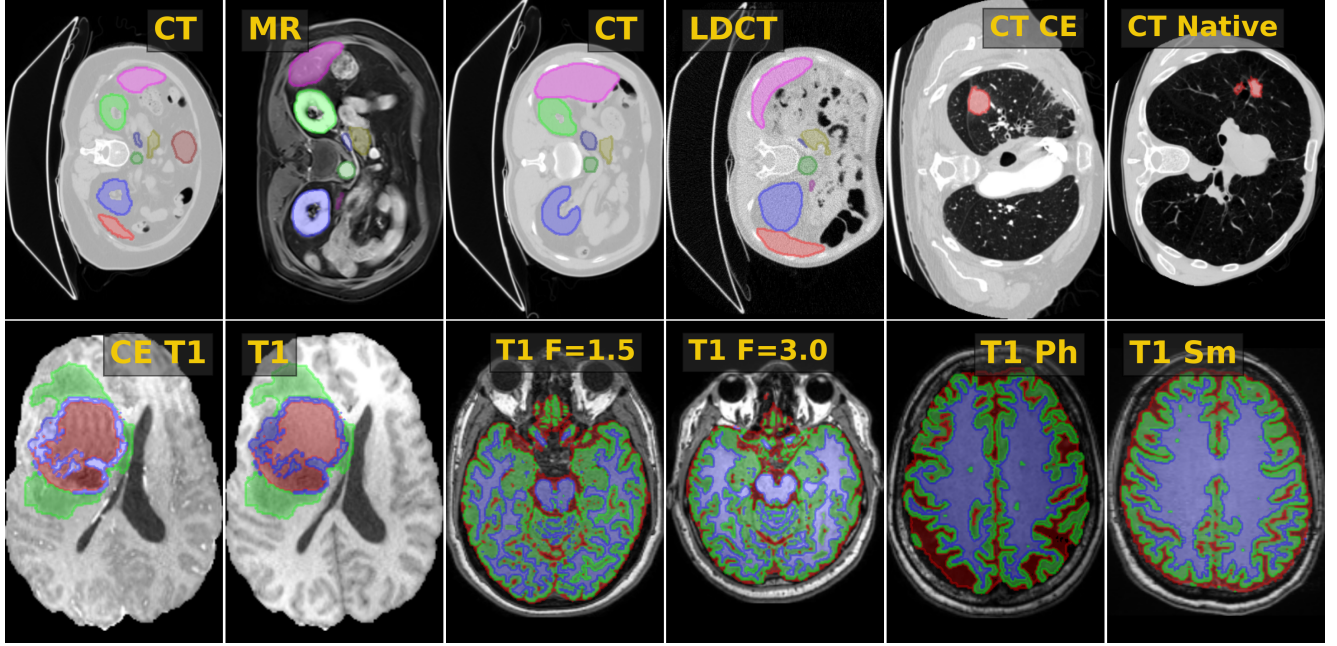


Figure 5. Examples from individual domains in M3DA with the corresponding segmentation masks. Left to right, top to bottom: CT to MR, CT to LDCT, CT CE to CT native, CE T1 to T1, T1 Field (1.5T to 3T), T1 Scanner (Philips to Siemens). Different colors correspond to different segmentation classes.

It includes 1308 studies (of which 1018 include CT studies) from 1010 patients. Lung’s nodules is one of the few clinical applications where both CE CT and CT are used, first for the initial scan, and second for the follow-ups [49]. We used LIDC for CE CT \rightarrow CT domain shift, we split data into three roughly equal groups, omitting scans with empty masks: contrast enhanced CT (source domain) X^s , CT without contrast enhancement X_{tr}^t (training part, target domain), and CT without contrast enhancement X_{ts}^t (test part, target domain). X_{tr}^t and X_{ts}^t were stratified by the number of lesions.

7. Methods details

7.1. UDA methods selection

Discrepancy-based approaches are based on incorporating maximum mean discrepancy measure as a regularization or auxiliary loss function [13, 40, 60]. These approaches were soon surpassed by simpler approximations, such as DeepCORAL [57]. However, all of them become computationally intractable due to significantly larger feature space in 3D segmentation task.

Since batch normalization (BN) [21] became the standard in DL, it allowed to reduce covariate shift by aligning first and second moments of feature distributions. But it introduced discrepancy between train and test by applying train-estimated statistics to the test samples. Here, *Adaptive BN (AdaBN)* [35] recalculates BN statistics on the unlabeled target data, helping to adapt to the target domain.

Contrary, *Instance Normalization (IN)* [62] was proposed for an efficient image stylization, and it calculates statistics for every input independently. This way IN might help adaptation, so we included IN to test it separately.

Selected methods: AdaBN, IN.

Self-training uses predicted pseudo-labels on the target data to regularize the downstream model. For instance, the authors of [11] proposed *self-ensembling (SE)* for visual DA. The same methodology was implemented for 3D medical image segmentation in [47]. The authors trained the first, student, network on the downstream task and updated the weights of the second, teacher, network via exponential moving average. They additionally imposed a consistency criterion: mean squared error between predictions of the two networks, thus, student network minimizes segmentation and consistency losses. We included SE with hyperparameters recommended in [47].

Specifically for semantic segmentation, training on self-generated predictions was shown to help in DA [83]. Later, the authors of [64] noted the connection between self-training and entropy minimization. They also showed that *minimizing the entropy (MinEnt)* of predictions surpasses self-training and other DA methods, so we included MinEnt in our benchmark.

Selected methods: SE, MinEnt.

Adversarial-based approaches form the basis for the most DA methods, as shown in [58]. The central idea is reversing the gradient from the domain classification network, thus learning domain invariant features for source and target inputs. To this end, the authors of [12] proposed *Domain Adversarial Neural Network (DANN)* for image classification, noting that their approach is generic and can handle any output label space. Consequently, DANN was implemented for DA in 3D medical image segmentation [26].

Although many other DANN modifications exist, e.g., decoupling feature encoders for source and target images [61] or connecting the domain classification network to the output layer [59], adapting them for 3D segmentation requires a separate effort. Hence, we focused on testing the core method and proceeded with the close to original DANN implementation of [26].

Selected methods: DANN.

Image-level adaptation is typically achieved using Generative Adversarial Network (GAN) [14]. The goal is to learn a mapping function between the source and target domains with a generator network. Then, one can use this generator to transfer images styles between domains. Specifically for UDA, the authors of [79] proposed *CycleGAN 2D* which additionally enforces the reconstruction loop consistency upon two generators. This method was also designed for 3D medical images in [76]; and it found numerous successful applications to medical image segmentation, e.g., top-3 solutions of the CrossMoDA challenge [10] used *CycleGAN 3D*. We included both approaches.

Image-level adaptation also includes non-generative approaches, such as Fourier Domain Adaptation (FDA) [72], where the style of images is changed by substituting their low frequencies in Fourier space. The authors of [74] succeeded in applying FDA to 3D medical image segmentation. However, such methods, similar to CT reconstruction kernel modulation [53], are not generic and heavily depend on modality-specific features, so we excluded them from further consideration.

Selected methods: CycleGAN 2D, CycleGAN 3D.

Preprocessing and augmentation are often overlooked when considering DA. On the one hand, we can standardize data characteristics by preprocessing, potentially reducing domain shift. We included two such steps by default: resampling to common spacing and intensity normalization; they are essential for the adequate model training [28]. Many studies demonstrated domain shift in medical images by intensity histograms [10, 47, 63]. Equalizing this difference might be of interest for adaptation, thus we included *histogram matching (HM)*.

On the other hand, augmentations can expand source distribution, potentially covering the target one. Here, nnUnet

framework [22] includes a variety of universal augmentations, so we tested them as a separate method under the name *nnAugm*. We also tested a commonly used and modality-agnostic *gamma correction augmentation (Gamma)* as an ablation study of nnAugm.

Finally, several advanced augmentation techniques were developed for domain generalization purposes. We included the most recent of them, *global intensity non-linear (GIN)* [44] and *modality independent neighborhood descriptor (MIND)* [68] augmentations.

Selected methods: HM, nnAugm, Gamma, GIN, MIND.

7.2. Implementation details

Table 10. Hyper-parameters.

hyper-parameter	nnUNet	U-Net (Baseline)
architecture	auto	auto
base features	32	24
normalization	instance (IN)	batch (BN)
batch size	2	2
patch size	(160, 192, 64)	(160, 160, 64)
epochs	600	600
batches per epoch	250	250
loss	Dice Loss + CE	Dice Loss + CE
oversampling rate	0.66	0.75
optimizer	SGD	SGD
momentum	0.99	0.99
weight decay	3×10^{-5}	3×10^{-5}
initial learning rate	10^{-2}	10^{-2}
learning rate schedule	poly decay	poly decay
learning rate decay power	0.9	0.9
test-time augmentation	✓	✗

We used an nnU-Net [22] backbone as segmentation network architecture in all methods. We preserved most of the nnU-Net training pipeline except for several methodological changes, which allow us to evaluate DA methods, such as AdaBN and InstanceNorm, separately and run the ablation studies. These changes along with the other training hyper-parameters are summarized in Table 10.

Firstly, we replaced the default InstanceNorm with BatchNorm layers and removed test-time augmentation, so we can compare different normalizations and adaptive normalizations (AdaBN) and assess the unhindered impact of DA methods. Secondly, we reduced the patch size and number of the network features, so all experiments fit in a single 16 GB NVIDIA Tesla V100 and our benchmark remains economical. We set the number of epochs to 600 in all experiments, so that any method could complete its training in three days.

Below, we provide DA methods implementation details:

Histogram matching uses the baseline training pipeline, except all image intensity histograms are equalized to an average histogram computed over the train set.

Gamma augmentation also uses the baseline training

pipeline, and we perform gamma correction with randomly selected $\gamma \sim U[0.5, 2]$ on every input image.

nnAugm similarly supplements the same baseline training with the original set of nnU-Net [22] augmentations.

InstanceNorm substitutes BN layers, while the training pipeline remains the same as in baseline.

Adaptive BN performs additional 1000 inference steps with batch size 4 over the baseline, updating the running statistics of BN layers on target training data.

Self-ensembling design and all parameters are reproduced from [47] with our architecture.

MinEnt adds a predictions entropy minimization criterion on target images. So we extended our training pipeline with the second step using target train images, and added entropy loss with the recommended in [64] weight $\lambda = 0.001$.

DANN introduces an auxiliary network called discriminator. Similar to recent studies [64], we used DCGAN [50] discriminator architecture, replacing 2D convolutions with 3D ones. The losses weighting parameter is taken from [26], e.g., $\alpha = 0.01$.

CycleGAN 2D is fully reused from the original study [79]. We trained a standalone CycleGAN 2D to map between source and target train images, where we sample axial slices from our volumetric images and rescale them into 256×256 gray scale images. Before predicting with the baseline segmentation model, we applied one of the generators to target test images (slice-by-slice) to transform them into fake source ones.

CycleGAN 3D is fully reused from the original study [76]. We trained a standalone CycleGAN 3D to map between source and target train images, where we sample patches of size (128, 128, 96) from our volumetric images. Before predicting with the baseline segmentation model, we applied one of the generators to target test images (via overlapping grid) to transform them into fake source ones.

GIN is fully reused from [44] with the implementation based on the nnU-Net framework.

MIND is fully reused from [68] with the implementation based on the nnU-Net framework.

All experiments are available and could be reproduced from <https://github.com/BorisShirokikh/M3DA-exp>.

8. Supplementary experiments

Firstly, Table 11 provides the results in four domain shift setups which we excluded from the benchmark. Differences in CT reconstruction kernels were excluded due to relative simplicity (Baseline is only marginally worse than the Oracle, and extensive augmentations almost closes this gap). We also excluded the domain shift between T1 and T2 MRI sequences, because, we were not able to find enough clinical justification for the inclusion.

Finally, example predictions for different DA methods are provided in Figure 7.

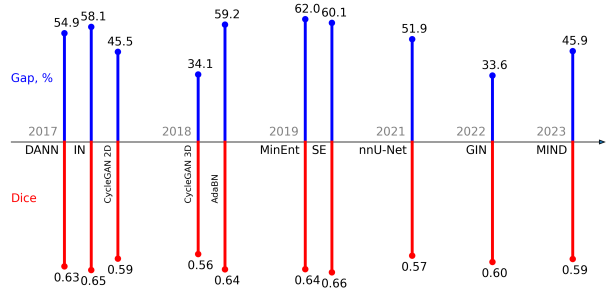


Figure 6. Average performance of domain adaptation approaches on M3DA benchmark; see Table 6 for detailed results.

Table 11. Four setups not included in the M3DA benchmark.

	CT (soft) \rightarrow CT (sharp)	CT (sharp) \rightarrow CT (soft)	T1 \rightarrow T2	T2 \rightarrow T1
Baseline	0.796	0.819	0.329	0.180
HM	—	—	0.246	0.031
MinEnt	—	—	0.322	0.094
CycleGAN 2D	—	—	0.425	0.080
AdaBN	—	—	0.262	0.067
DANN	—	—	0.228	0.028
IN	—	—	0.243	0.038
Gamma	—	—	0.288	0.132
SE	—	—	0.000	0.000
nnAugm	0.844	0.822	0.327	0.197
Oracle	0.847	0.845	0.728	0.686

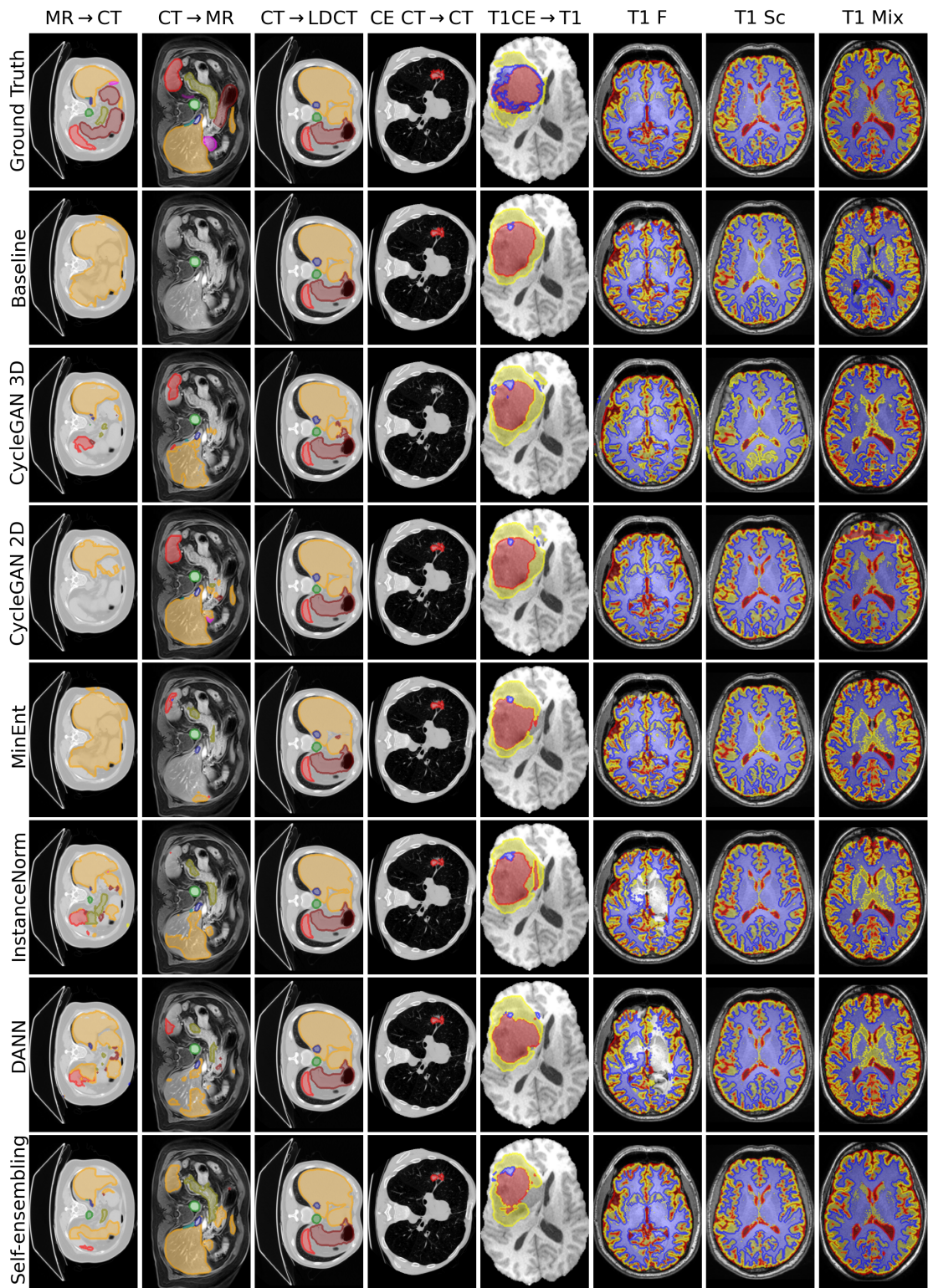


Figure 7. Example predictions for different DA methods. Methods are in rows, starting with ground truth in a first row. All eight benchmark tasks are in columns.